Title: Jupiter's X-ray and EUV auroras monitored by Chandra, XMM-Newton, and Hisaki satellite

Authors: T. Kimura[1,2,3]*, R. P. Kraft[3], R. F. Elsner[4], G. Branduardi-Raymont[5], R. Gladstone[6], C. Tao[7], K. Yoshioka[1], G. Murakami[1], A. Yamazaki[1], F. Tsuchiya[8], M. F. Vogt[9], A. Masters[10], H. Hasegawa[1], S. V. Badman[11], E. Roediger[12], Y. Ezoe[13], W. R. Dunn[5], I. Yoshikawa[14], M. Fujimoto[1, 15], and S. S. Murray[3]

Key points:

- Count rate of Jupiter's X-ray aurora is positively correlated with the solar wind velocity
- Source field line of Jupiter's X-ray aurora magnetically map to the pre-noon to post dusk sector
- The magnetopause reconnection and/or KH instability could drive Jupiter's X-ray aurora

Affiliations:

[1]Institute of Space and Astronautical Science, Japan Aerospace Exploration Agency, Sagamihara, Japan.

[2]Nishina Center for Accelerator-Based Science, RIKEN, 2-1, Hirosawa, Wako, Saitama, Japan

[3]Harvard-Smithsonian Center for Astrophysics, Smithsonian Astrophysical Observatory, Cambridge, MA, US

[4]NASA Marshall Space Flight Center, Huntsville, Alabama, US

[5]Mullard Space Science Laboratory, University College London, Holmbury St Mary, Dorking, Surrey RH5 6NT, UK

[6]Department of Space Studies, Southwest Research Institute, Boulder, Colorado, USA.

[7]Institut de Recherche en Astrophysique et Planétologie, Université de Toulouse, CNRS, Toulouse, France.

[8]Planetary Plasma and Atmospheric Research Center, Tohoku University, Sendai, Japan

[9]Center for Space Physics, Boston University, Boston, Massachusetts, USA

[10]Department of Physics, Faculty of Natural Sciences, Imperial Collage London, UK

[11]Department of Physics, Lancaster University, Bailrigg, Lancaster LA1 4YB, UK

[12]Hamburger Sternwarte, Universität Hamburg, Gojensbergsweg 112, 21029, Hamburg, Germany

[13]Tokyo Metropolitan University, Tokyo, Japan

[14]Department of Complexity Science and Engineering, The University of Tokyo, Chiba, Japan

[15]Earth-Life science Institute, Tokyo Institute of Technology

*Correspondence to: tomoki.kimura@riken.jp

Abstract:

Jupiter's X-ray auroral emission in the polar cap region results from particles which have undergone strong field-aligned acceleration into the ionosphere [*Cravens et al.*, 2003]. The origin of precipitating ions and electrons and the time variability in the X-ray emission are essential to uncover the driving mechanism for the high energy acceleration. The magnetospheric location of the source field line where the X-ray is generated is likely affected by the solar wind variability. However, these essential characteristics are still unknown because the long-term monitoring of the X-rays and contemporaneous solar wind variability has not been carried out. In

Apr 2014, the first long-term multi-wavelength monitoring of Jupiter's X-ray and EUV auroral emissions was made by the Chandra X-ray Observatory, XMM-Newton, and Hisaki satellite. We find that the X-ray count rates are positively correlated with the solar wind velocity and insignificantly with the dynamic pressure. Based on the magnetic field mapping model, a half of the X-ray auroral region was found to be open to the interplanetary space. The other half of the X-ray auroral source region is magnetically connected with the pre-noon to post-dusk sector in the outermost region of the magnetosphere, where the Kelvin-Helmholtz (KH) instability, magnetopause reconnection, and quasi-periodic particle injection potentially take place. We speculate that the high energy auroral acceleration is associated with the KH instability and/or magnetopause reconnection. This association is expected to also occur in many other space plasma environments such as Saturn and other magnetized rotators.

Main Text:

1. Introduction

Jupiter is the brightest X-ray emitting planet in our solar system, and the most intense X-ray source region at Jupiter is the polar auroral region [*Bhardwaj and Gladstone*, 2000; *Bhardwaj et al., 2007* and references therein]. The X-ray emission from Jupiter's polar region was discovered by the Einstein X-ray satellite [*Metzger et al.*, 1983]. Recent space telescopes have investigated its spectra and time variability. Using imaging by the High Resolution Camera (HRC) onboard Chandra X-ray Observatory (CXO), *Gladstone et al.* [2002] indicated the origin of the auroral X-rays is confined to a 'hot spot' in the polar cap region. The hot spot pulsed with a period of ~40 minutes. This periodicity was not unambiguously detected in more recent observations [*Branduardi-Raymont et al.*, 2004, 2007; *Elsner et al.*, 2005]. *MacDowall et al.* [1993] and

McKibben et al. [1993] discovered 40 minute periodic radio bursts (QP bursts) emitted from the polar region in the same phase with relativistic electron outbursts at > 8 MeV. *MacDowall et al.* [1993] indicated that day-to-day variability in the occurrence probability of QP bursts is correlated with the solar wind velocity. *Kimura et al.* [2010] suggested that the source field lines of QP radio bursts extend to the outermost region of the magnetosphere or interplanetary space.

These polar X-ray and radio emissions are suggestive of energetic upward and downward particle acceleration in the polar cap region that can be driven by the external solar wind condition. A day-to-day variability is expected for the X-ray aurora. *Hui et al.* [2010] showed evidence for temporal variability in auroral spectra depending on observation date. However, there have been no long-term continuous observations by X-ray telescopes that can reveal the timescale of solar wind-induced variability in X-rays.

Einstein, CXO, and XMM-Newton made spectral measurements of Jupiter's X-ray aurora [e.g., *Metzger et al.*, 1983; *Elsner et al.*, 2005; *Branduardi-Raymont et al.*, 2004, 2007, 2008]. Auroral spectra are dominated by soft X-ray emission at < 2 keV. These spectral measurements indicate strong soft X-ray emission around 0.5-0.8 keV energy band which is suggestive of the highly charged oxygen line emission at OVII and/or OVIII. Additional line emissions of highly charged sulfur and/or carbon were suggested at 0.25-0.35 keV [*Elsner et al.*, 2005]. Above 2 keV, continuum emission is dominant, and has been interpreted as electron bremsstrahlung [*Branduardi-Raymont et al.*, 2004, 2007, 2008]. Imaging spectroscopy using the Advanced CCD Imaging Spectrometer (ACIS) onboard CXO showed that the soft X-rays below 2 keV are emitted from the polar cap region [*Branduardi-Raymont et al.*, 2008] which is close to the hot spot discovered by *Gladstone et al.* [2002]. The hard X-rays above 2 keV have footprints on the planet coincident with the main oval emission in the ultraviolet (UV) wavelengths. The main oval emission is excited through the collisions of atmospheric hydrogen with precipitating energetic electrons associated with the magnetosphere-ionosphere coupling currents [e.g., *Cowley and Bunce*, 2001; *Hill*, 2001].

The soft X-ray radiative process of precipitating ions undergoing charge exchange with the neutral atmospheric particles has been numerically modeled [*Kharchenko et al*. 1998, 2006, 2008; *Hui et al.* 2009, 2010; *Ozak et al.*, 2010, 2013; *Cravens et al.*, 1995, 2003]. *Kharchenko et al*. [1998, 2006, 2008], *Hui et al.* [2009, 2010], and *Ozak et al.* [2010, 2013] modeled the X-ray spectral lines emitted via the collisional excitation between ions and neutrals based on the Monte Carlo simulation. From comparison of modeled synthetic spectra with the observed spectra, averaged ion energies are determined to line between 1 and 2 MeV/amu [*Kharchenko et al.*, 2008].

Cravens et al. [2003] discussed two scenarios for the origin of the precipitating ions: the magnetospheric plasma on closed field lines and solar wind plasma on open field lines. A magnetospheric origin requires acceleration by at least an 8 MV field aligned potential drop in order to account for the observed X-ray intensity and spectrum. A solar wind origin requires a smaller potential drop, ~200 keV, for oxygen ions. The smaller potential drop in this case follows because the solar wind oxygen ions are in higher charge states than the magnetospheric oxygen ions. *Cravens et al.* [2003] concluded that the magnetospheric scenario is more likely than the solar wind scenario to account for the magnetosphere-ionosphere coupling theory, observed spectral features of the X-ray aurora, and proton auroral precipitation accompanying the oxygen precipitation. Some fitting of the modeled spectra to observed spectra indicated that the oxygen ion emission lines are dominant for soft X-ray while there is no significant contribution by carbon lines [*Hui et al.*, 2009, 2010]. This further suggests the precipitating ions originate from the magnetosphere rather than the solar wind because carbon ions are more abundant in the solar wind than in the magnetosphere.

Thus previous works suggest that the energetic ions causing the X-ray aurora originate from the outermost region of the magnetosphere and/or interplanetary space where some acceleration driving mechanisms occur, possibly under the influence of the solar wind. However, this suggestion has not been tested observationally because there has been no long-term monitoring of the X-ray aurora over the weeks or months time scale associated with solar wind variability. A complete study also requires simultaneous monitoring of the outermost magnetospheric and solar wind variability.

Such long-term observations of Jupiter's X-ray aurora were carried out during a multi-wavelength observing campaign for Jupiter's magnetosphere from Apr 8 to 24, 2014. CXO, XMM, Hisaki satellite, Suzaku, and other ground-based facilities monitored Jupiter's aurora, plasma torus, and radiation belts from X-ray to radio wavelengths. In the present study, we focus on the datasets from CXO, XMM, and Hisaki. CXO provides highly resolved X-ray images in order to determine the X-ray source location. XMM-Newton provides X-ray spectral imaging in order to investigate the ion auroral emission. Hisaki provides imaging spectra of the electron extreme ultraviolet (EUV) auroral emission. Temporal variability is extracted from each telescope's dataset.

This study addresses day-to-day variability, spectral features, and source locations of the X-ray aurora based on the long-term observations compared with the modeled solar wind conditions for the first time. We discuss precipitation ion origin and acceleration mechanisms based on these long-term observations.

The NASA JUNO mission is going to start in-situ measurements in the polar magnetosphere after the Jupiter Orbit Insertion in the last half of 2016 [e.g., *Bagenal et al.*, 2014]. The electromagnetic (EM) field and energetic particles directly measured by JUNO above the polar cap region will give us pivotal clues to the particle species and associated plasma microphysics of the energetic acceleration. This study complementally reveals the global distribution and long-term variability of the energetic acceleration based on remote monitoring of the X-ray and EUV auroras.

2. Dataset

The Chandra High Resolution Camera (HRC) [*Murray et al.*, 2000] covers the 0.1-10 keV band, with spatial resolution of 0.4 arcsec (~1500 km at Jupiter's surface during this period), high time resolution, and an effective area of 227 cm^2 at 1 keV photon energy. Six exposures each with a duration of ~40 ks were taken on Apr 8, 10, 12, 15, 17, and 20 2014. In the present study the X-ray source distribution in the northern auroral region is analyzed. Data reduction of the northern auroral image and its temporal variability is described in the sections below.

The XMM-Newton European Imaging Camera (EPIC) PN detector [*Strüder et al.*, 2000; *Turner et al.*, 2000] performs imaging spectroscopy over the energy band 0.15-12 keV. The spatial resolution, as measured by the half energy width (HEW), is 15 arcsec, and the spectral resolution is 80 eV at 1 keV. Two exposures with a duration of 40 ks were performed on Apr 15 and 20 2014, respectively. Data reduction of spectra and analysis of temporal variability are described in the Sections 3 and 4.

The EXtreme ultraviolet spectrosCope for ExosphEric Dynamics (EXCEED) [*Yoshioka et al.*, 2013] onboard Hisaki measures EUV photons, which are combined into spatio-spectral images with 1024×1024 pixels with 10 minute exposure time. The spectral range extends from 470 to 1530 Å. The total spatial resolution is 17 arcsec. The dumbbell-shaped slit with a width of 140 arcsec was positioned on the northern aurora during the present observing campaign. Hisaki observed Jupiter for 40 min out of every 100 min orbit, for the longest continuous period for the three space telescopes discussed here spanning an observation period spans from Apr 10 to 24 2014. Time variations in the total emitted power at 900-1480 Å were extracted from the imaging spectra as described in *Kimura et al.* [2015].

There was no solar wind monitor near Jupiter during the present observing campaign. We estimate the solar wind variation at Jupiter using a 1D magnetohydrodynamic (MHD) model that propagates the solar wind measured at the vicinity of Earth [*Tao et al.*, 2005]. Based on the solar wind observations by the Ulysses spacecraft, the accuracy of the arrival time of dynamic pressure pulses with large amplitudes of > 0.25 nPa was found to be within 48 hours when $|\Delta\Phi| < 50°$, where $\Delta\Phi$ is the Earth-Sun-Jupiter angle. In the present study, $\Delta\Phi$ is estimated to be 85-99° from Apr 8 to 24, suggesting the uncertainty in the arrival time to be larger than 48 hours.

3. Imaging and spectroscopy of X-ray aurora

The X-ray source distribution in the northern auroral region is measured by HRC. X-ray positions measured in the detector frame are converted to the Jupiter-centered frame as indicated in Figure 1a. Then these events are mapped onto Jupiter's surface using the method described by *Elsner et al.* [2005].

Figure 2 is a polar plot of the auroral photons detected in the northern hemisphere, where the background colored contours indicate the magnitude of the magnetic field strength. The field strength is provided by the internal field VIPAL model [*Hess et al.*, 2011]. Orange, blue, and white lines indicate footprint latitudes for the magnetic shells that correspond to equatorial radii of 15, 30, and 120 Rj (Rj: Jovian radii, 71492 km), respectively. Mapping of these radial distances to the polar ionosphere was performed using the *flux equivalence mapping model* developed by *Vogt et al.* [2011, 2015]. As reported in previous observations by *Gladstone et al.* [2002], *Elsner et al.* [2005], and *Branduardi-Raymont et al.* [2008], most of the X-ray photons are confined in the spot-like region at higher latitudes than the footprint latitude of the magnetic shell corresponding to 30 Rj. The latitudes corresponding to 30 Rj are close to the main UV auroral oval that is magnetically connected to the middle magnetosphere. Based on the equatorial mapping which will be described in Section 5, we conclude that the X-ray source region is magnetically connected with the outer region of the magnetosphere.

We morphologically divide the northern auroral hot spot into two regions. In the ‘core‘ region where 54% of the total auroral photons are concentrated within a small circle centered at 165° in System III (SIII) longitude and 65° in latitude with a 6.5° radius on Jupiter’s surface, indicated by the red points in Figure 2. The ‘halo‘ region which surrounds the core region, containing 46% of the total auroral photons within an annulus centered at 170° in SIII longitude and 69° in latitude with a 15° outer radius and 6.5° inner radius, indicated by the blue points in Figure 2.

We extract X-ray spectra of the northern aurora from the EPIC-pn imaging spectral data. The Jupiter-centric EPIC-pn image is shown in Figure 1b. A green rectangle is centered on Jupiter’s north pole. The long side of the green rectangle is parallel to Jupiter’s equator. Photons from within the green rectangle are dominated by the X-ray aurora. Due to the 15 arcsec angular resolution of the EPIC-pn, the solar X-rays reflected from Jupiter’s disk contaminate the auroral spectra. For the 2003 observation, *Branduardi-Raymont et al.* [2007] estimated the contamination at 7.8 %. We regard this estimate as approximately valid for the present case because of the similar phase in solar activity. The EPIC-PN detector is sensitive to cosmic rays that mimic X-ray events and are responsible for the background noise. The total background count rate and spectra are estimated using the area within the green circle in Figure 1b, rescaled to the area of the auroral region and subtracted from the auroral count rate and spectra. The diffuse X-ray sky background is also included in the total background but not in the auroral image because Jupiter's disk occults the sky. Due to this effect, the background-subtracted auroral count rate is underestimated due to the sky background. However, this underestimation does not affect investigation of the day-to-day relative variability in the X-ray count rate.

The background-subtracted auroral spectra are plotted in Figure 3. The Apr 15 spectrum (Figure 3a) peaks at 0.5-0.9 keV, suggestive of the oxygen lines found in *Branduardi-Raymont et al.* [2004, 2007, 2008] and *Elsner et al.* [2005]. The Apr 20 spectrum (Figure 3b) peaks at 300-400 eV. This photon energy band corresponds to the emission lines of sulfur and carbon [*Elsner et al.*, 2005]. A Gaussian line at 570 eV and the VAPEC model, which is a collisional equilibrium plasma emission model implemented in the astronomical X-ray spectral fitting tool XSPEC [Arnaud, 1996], are fitted to the observed spectra to estimate the photon flux, as indicated by the black solid lines in Figure 3. Free parameters are intensity of 570 eV Gaussian, plasma temperature, abundance of atoms in the plasma, and column density of the plasma in the VAPEC model. The reduced χ^2 values are estimated to be 1.0 and 0.96 with 52 and 41 degrees of freedom for the Apr 15 and 20 spectra, respectively. Probabilities of chance occurrence for χ^2 values greater than the best-fit values are 41% and 54%, respectively, so these are acceptable fits. Although the VAPEC model is not physically consistent with the auroral X-ray emission, which after all are due to charge exchange and bremsstrahlung [e.g., *Cravens et al.*, 2003; *Branduardi-Raymont et al.*, 2008], the model does describe well the observed spectral shapes. Based on these fits, we estimate photon fluxes of 1.0×10^{-4} and 8.6×10^{-5} photons/cm^2/s at 0.3-2 keV for Apr 15 and 20, respectively. We also estimate the energy flux of 1.1×10^{-16} and 7.3×10^{-17} W/m^2 at 0.3-2 keV for Apr 15 and 20, respectively. These energy fluxes correspond to the total radiated power of ~0.89 and ~0.59 GW in this analysis period. The total radiated power is within the typical range 0.4-1.0 GW reviewed by *Bhardwaj et al.* [2007]. There is a weak peak around 1.4 keV on

Apr 15 and 20, suggestive of Mg XI line at 1.35 keV as indicated by *Branduardi-Raymont et al.* [2007]. This could be solar photons reflected at Jupiter's disk region.

4. Day-to-day variability in EUV and X-ray aurora

We now turn to time variability of the X-ray auroras. For the CXO images, we extracted count rates from the entire region of the northern hot spot, including both the core and halo regions. For the XMM images, we extracted count rates from the northern polar region for the energy bands 0.5-0.7 keV, which includes the oxygen ion lines, and 0.3-0.5 keV, which includes the carbon and sulfur lines.

Figure 4 displays the time variations in EUV and X-ray aurora, and in the solar wind. We extracted the 900-1480 Å EUV emission power, in 10 minute intervals, from the EXCEED data using the method described by *Kimura et al.* [2015]. We restricted this analysis to times when the Central Meridian Longitude (CML) for the Hisaki spacecraft fell in the interval 100°-250°. This restriction removes modulation at Jupiter's rotation period. The CXO-HRC core and halo count rates shown in Figure 4b are averaged over each ~40 ks observation. The XMM-Newton/EPIC-pn count rates shown in Figure 4c and d are also averaged over ~40 ks. Error bars in these X-ray count rates correspond to one sigma value evaluated by the Poisson statistics.

The EUV auroral total power (Figure 4a) shows gradual variations on a timescale of a few days with peaks on day 101, 105, 107 and 109. *Kimura et al.* [2015] suggested that increases are associated with the compression of the magnetosphere by a dynamic pressure enhancement. The increases on days 101, 105, 107 and 109 are ~150, ~100, ~200 and ~400 GW, respectively, above the emission levels during periods when the solar wind is quiet. Over ~2 days emission levels decayed down to quiet levels. The UV and infrared (IR) auroral intensities have been reported to vary in response to compression by the solar wind [e.g., *Baron et al.*, 1996; *Pryor et al.*, 2005; *Nichols et al.*, 2007, 2009; *Clarke et al.*, 2009; *Kimura et al.*, 2015]. The peaks, followed by the decays, on day 107 and 109 appear to be associated with the adjacent compressional regions arriving on days 105 and 109 in the MHD simulation. This implies the uncertainty in the propagated solar wind arrival time to be ~48 hours or less during this observation period.

The CXO/HRC auroral core data shown in Figure 4b (red circles) exhibit variability of a factor ~4 over a ten day period. The count rate gradually decreases from the highest value of 0.0015 counts/sec on day 100 to the lowest value of 0.0004 counts/sec on day 110, and is positively correlated with the simulated solar wind velocity. We estimate the cross correlation coefficient (CCC) for the core count rate and solar wind velocity. In this analysis, the solar wind velocity is averaged over ±48 hours from the count rate measurement time to take the 48-hour uncertainty in the solar wind arrival time into account. For correlation with time lags, the core count rate is temporally lagged before the averaging. CCC reaches +0.94 when the time series of the count rate are lagged by 27 hours. Magnitude of this CCC is the largest value for time lags from -48 to +48 hours. The 27-hour time lag is significantly less than the 48-hour uncertainty in the solar wind arrival time. Figure 5a is a scatter plot of the X-ray count rate and solar wind velocity for CCC=+0.94. The error bars in the velocity are standard deviations of the time series that span ±48 hours from the count rate measurement time. The error bars in the count rate are estimated based on the photon statistics the same as in Figure 4. The positive gradient of data points is significant with respect to the estimated errors. We conclude the core count rate is positively correlated with the solar wind velocity with a time lag less than the solar wind arrival uncertainty.

The correlation of the core count rate with the dynamic pressure is shown in Figure 5b. The largest magnitude CCC is estimated to be +0.48 with a time lag of 36 hours. The time lag is significantly less than the 48-hour solar wind uncertainty. However, the positive gradient of data points does not exceed the estimated error bars, which is suggestive of insignificant correlation.

The count rate for the halo region also appears weakly correlated with the solar wind parameters. The variability in the count rate is weaker (0.0006-0.0011 counts/sec). The largest magnitude CCC of the halo with the solar wind velocity is +0.89 of which gradient significantly exceeds the error bars as shown in Figure 5c, but with a larger time lag of 48 hours. In view of the time lag for the solar wind velocity compared with a ~48 hour arrival time accuracy, we consider the correlation of the halo with the solar wind velocity is less convincing than the core count rate. Figure 5d indicates that the correlation of the halo count rates with the dynamic pressure is insignificant as well as the core. The largest magnitude CCC is +0.45 with a lag of 46 hours.

The XMM-Newton/EPIC-pn oxygen band count rate (0.5-0.7 keV) shown in Figure 4c shows a decrease from 0.018 counts/sec on day 106 to 0.01 counts/sec on day 110, a change of 44%. This decrease of 8×10^{-3} counts/sec is significantly larger than the estimated error of 9×10^{-4} counts/sec. Although we have only two EPIC-pn data points, this decrease is consistent with the CXO/HRC count rate decreases for the core and halo. The EPIC-pn count rate in the carbon and sulfur band at 0.3-0.5 keV shows a smaller decrease from 0.0092 counts/sec on day 106 to 0.0060 counts/sec day 110, a change of 35%. This decrease is 3.2×10^{-3} counts/sec, which is also larger than the estimated error of 0.8×10^{-3} counts/sec.

5. Local time distribution of the source field lines

The 0.4 arcsec HRC spatial resolution enables accurate X-ray source locations. Using the *Vogt et al.* [2011, 2015] *flux equivalent mapping model*, we determined the equatorial mapping of the northern auroral X-rays. The flux equivalence model requires that the magnetic flux through a given region in the ionosphere equals the magnetic flux trough the region to which it maps in the magnetosphere. Conserving this equivalence, the mapping of the magnetic flux tube is iteratively carried out from the inner magnetic shell at Ganymede's orbit (15Rj) to the outermost radial distance of 150 Rj. Due to the high latitude of the X-ray aurora, some photons map to distances outside the *Joy et al.* [2002] uncompressed magnetopause for a dynamic pressure of 0.04 nPa.

Figure 6 shows the distribution of equatorial mappings in Jupiter-Sun-Ecliptic (JSE) coordinates for the 49% of X-rays that map inside the magnetopause. The other 51% map to open field lines beyond the magnetopause and therefore are not shown in Figure 6. Red and blue crosses correspond to the core and halo regions, respectively. X-rays from the core map very close to the nominal location of the magnetopause in the pre-noon to post-dusk sector. X-rays from the halo region show a broader distribution over the region from close to Jupiter to the outermost regions of the magnetosphere, from the nose at noon (~90 Rj) to the distant tail region (~100 Rj) in the post-dusk sector.

Figure 7 shows the local time (LT) distribution of the X-ray mapping into the equatorial plane. We exclude mappings onto field lines beyond 90 Rj. This is because these field lines are not closed at all LT: e.g., the field lines beyond 90 Rj in the noon sector are open and do not map to the equatorial plane. This exclusion reduces any bias due to the mapping capability of the model. Figure 7a shows stacked histogram distributions in LT of the closed field lines for the halo (blue) and core (red), respectively. Both the halo and core region are significantly populated in the pre-noon to dusk sector with the peak at LT 12-13. Figure 7b shows the LT distribution of the X-ray occurrence probability. The black broken line histogram is the cumulative observation time as a function of LT, which is normalized by the peak value at LT 12-13. The cumulative time is evaluated as follows: 1. The visible time of the polar cap region is temporally integrated over the observation period. 2. The distribution of the visible time in the polar cap is mapped onto the equatorial plane. 3. The mapped visible time is spatially integrated over radial distances at 15-90 Rj at each LT sector. There is significant cumulative observation time even in the midnight sector (e.g., 35% of the maximum visible time in LT 0). This is because the entire northern polar cap region is visible from the observer when Jupiter's magnetic north pole faces toward the observer. The observer direction approximately corresponds to the sun direction in this analysis period. Thus footprints of the all LT sector are visible for the observer as indicated in Figure 9 of *Vogt et al.* [2011]. The occurrence probabilities for the halo and core are given by dividing the number of the source field lines by the cumulative observation time. These probabilities are shown as blue and red histograms in Figure 7b. These occurrence probabilities are normalized by the peak values at LT 12. The noon-to-dusk population is clearly larger than the dawn population. These statistics indicate that the X-ray source field lines are more populated at dusk than at dawn.

Figure 8 indicates the distribution of CML where CXO observed the X-ray photons emitted from the closed field lines mapping onto the equatorial distance of 15-90Rj. The format is similar to that of Figure 7. The observation time is cumulated at each CML when the polar cap region is visible from the observer. In contrast to the LT statistics, Figure 8b shows that the cumulative observation time is restricted in the CML range of 60°-360°. This is because the north polar cap region is the most visible from the observer when the magnetic north pole faces toward the observer, approximately corresponding to CML~200°, whereas it is invisible around CML~20° when the magnetic north pole faces the anti-observer direction. The occurrence probabilities for the halo and core are populated in a range from 60° to 300°. From 60° to 150° when the polar cap region appears at the dayside from the nightside, sum of the occurrence probabilities increases from 0 up to 1. This accompanies the increase in the cumulative observation time from 0 to 0.75, which means that the polar cap region changes to frequently visible from completely invisible. We interpret the increase in the occurrence probability as the increase in apparent area of the X-ray source location seen from the observer. There could be the increase in the X-ray photon emission rate simultaneously with the apparent increase of the X-ray source area. However, this effect cannot be separated from the increase in the apparent area. From 150° to 270° when the entire polar cap region is in the dayside, the total occurrence probability decreases from 0.7 to 0.18. The cumulative observation time is constantly high (~0.78-1) which means that the polar cap region is constantly visible from the observer. This suggests that the decrease in the occurrence probability is not the apparent area decrease but decrease in the X-ray emission rate. In other words, the X-ray emission rate is likely modulated depending on Jupiter's rotation. From 270° to 360° when the polar cap region goes to the nightside from the dayside, the total occurrence probability decreases from 0.18 down to 0. The cumulative observation time decreases from 0.8 to 0.38, which means the decrease of visible area in the polar cap. The decrease in the occurrence probability can be interpreted that the X-ray emission rate decreases and/or the apparent area decreases.

6. Discussion

6.1. Temporal variability

From the time variability shown in HRC data (Figure 4b and Figure 5a), we found that the count rate of the core X-ray auroral region is positively correlated with the simulated solar wind velocity, while the halo count rate is correlated with the velocity at lower significance. This makes sense since the core is magnetically connected with the boundary of the magnetosphere (see Figure 6), where the magnetosphere is easily affected by the solar wind variability than the closed region well inside the magnetosphere.

The EPIC-pn 0.5-0.7 keV count rate, mostly due to oxygen line emission, shows a gradual decrease over time. On the other hand, the EPIC-pn 0.3-0.5 keV count rate, presumably due to carbon and sulfur line emission, shows less variability. Based on imaging spectral observations by the ACIS onboard Chandra, *Dunn et al.* [under review] found the oxygen line dominates in the core region during the solar coronal mass ejection impact on Jupiter, while the sulfur and carbon lines dominate at lower latitudes. Although the particle origin of the oxygen emission is still unclear, *Dunn et al.* [under review] suggested that oxygen ions originating from either the magnetosphere and/or solar wind along the magnetospheric boundary will precipitate into the core region. Our study also implies the oxygen ions have variability possibly associated with the solar wind. The sulfur ions will originate from the outer magnetosphere along the field lines connected with the halo region.

Previous monitoring the day-to-day auroral variations in the radio, infrared (IR) and UV wavelengths reported the correlation with the dynamic pressure [e.g., *Baron et al.*, 1996; *Waite et al.*, 2001; *Prangé et al.*, 2001, 2004; *Gurnett et al.*, 2002; *Nichols et al.*, 2007, 2009; *Kimura et al.*, 2015]. Most of these studies associated this correlation with the magnetospheric compression by the interplanetary shock followed by the upward auroral current enhancement, corresponding to acceleration and precipitation of the magnetospheric electrons. This study now suggests that the core region emission is correlated with the solar wind velocity. If the core X-rays are emitted due to charge exchange between downward accelerated ions and atmospheric atoms, then the positive correlations of the core count rates with the solar wind velocity are suggestive of the auroral downward current associated with the solar wind velocity.

Saturn also has a corotation-powered magnetosphere, and *Galopeau et al.* [1995] and *Cecconi and Zarka* [2005] modeled the source location and periodicity in the intensity of Saturn's auroral kilometric radiation (SKR). They concluded that their results were consistent with the Kelvin-Helmholtz (KH) instability, for which growth rate increases with increased velocity shear between flows inside and outside the magnetopause. In their picture, the sector containing the SKR source region is the same as the LT sector where the KH instability is theoretically viable. They found that the spatial extent of the KH viable region and its dependence on the solar wind velocity matches well with the observed beaming, periodicity, and spectrum. In the case of Jupiter, if the velocity shear at the magnetopause depends strongly on the solar wind velocity, then the positive correlation of the X-ray emission with the solar wind velocity is consistent with the theoretical growth rate of the KH instability. We therefore speculate that the core region X-ray emission is modulated by the upstream solar wind velocity and by velocity shear at the magnetospheric boundary region. In this case the precipitating oxygen ions could be from a mixture of the solar wind and magnetospheric plasmas.

Figure 8 shows the dependence of the X-ray occurrence probability on CML: i.e., Jupiter's rotation. Although the variability is likely attributed to the visibility of the X-ray source area, the dependence of the X-ray emission rate on the rotation is also implicated. The dependence on the rotation has long been reported from the observations of QP bursts [*MacDowall et al.*, 1993; *Morioka et al.*, 2006; *Kimura et al.*, 2008, 2010, 2012]. The rotation dependences of the X-ray and radio are suggestive of the auroral accelerations in the polar cap region organized by Jupiter's rotation.

6.2. Possible driving mechanism

We found that the X-ray source magnetically connects with the outermost region of the magnetosphere (Figure 2). In the equatorial plane, source field lines are populated from the pre-noon to post-dusk sector (Figure 6 and Figure 7). This pre-noon to post-dusk population is consistent with the observation fact that QP bursts and synchronized relativistic electron bursts have been observed at southern high latitudes (~-40°) around the dusk terminator [*MacDowall et al.*, 1993]. *Bonfond et al.* [2011] reported that the pulsating UV aurora with 2-3 minute period in the polar cap region is magnetically connected with the radial distances of 55-120 Rj at LT 10-18 hours in the equatorial plane. We expect the source location of QP bursts, MeV electron bursts, and pulsating UV aurora coincide with that of the X-ray aurora. This pre-noon to post-dusk distribution is similar to the statistical local time distribution of the quasi-periodic MeV electron injections with 60 minute period, which was recently found by Cassini in the middle to outermost region of Saturn's magnetosphere [*Roussos et al.*, 2015]. This strongly suggests that both Jupiter's and Saturn's magnetospheres have similar energetic particle accelerations in the pre-noon to post-dusk sector. Further investigations of any quasi-periodicity in the X-ray and UV auroras at Jupiter compared to particle injections at Saturn could illuminate the potentially common acceleration process.

Theories have long predicted the KH instability at the dawn flank of Saturn's magnetosphere due to the larger velocity shear there than at the dusk [*Galopeau et al*., 1995; *Cecconi and Zarka*, 2005; *Desroche et al.*, 2013]. However, the KH instability-like signatures have been actually detected at the dusk side by *in-situ* magnetic field measurements [*Masters et al.*, 2012a; *Delamere et al.*, 2013]. The surface wave or bipolar fluctuations in the azimuthal and radial magnetic field components that could be due to the KH instability were detected in the outermost region of Saturn's magnetosphere. Most of the events were found on the dusk flank, contrary to the theoretical expectation. Although there is still this discrepancy between the theoretical and observational LT location, the hybrid simulation carried out by *Delamere et al.* [2013] showed that the field aligned currents and bidirectional field aligned electron beams are significantly generated if the KH instability occurs. The KH-like events on the dusk flank at Jupiter could then generate polar auroral variations. However, more work is required to determine if the KH-like events can actually establish the field aligned potential drops up to several megavolts as required by auroral theories [*Cravens et al.*, 2003].

The region where magnetopause reconnection is preferably excited was also predicted to be at the noon to dusk sector [*Desroche et al.*, 2012], under the condition that the plasma β value is ~10 inside the magnetopause. The viable region was determined by the theoretical limit on steady reconnection formulated by *Swisdak et al.* [2010]. However, the efficiency of steady reconnection is theoretically reduced for large velocity shear at the reconnection site [*Cassak and Otto*, 2011]. This seems inconsistent with the correlation of the X-ray emission with the solar wind velocity as found in the present study.

This discrepancy could be resolved by intermittent reconnection. *Bunce et al.* [2004] proposed that the magnetopause reconnection under 'fast' solar wind conditions can establish strong field aligned currents and resultant field aligned accelerations with several megavolt potential drop. This is consistent with fact that in the present study the core count rates are more sensitive to the solar wind velocity than the halo count rates. Observations and numerical simulations and observations for Earth [*Raeder et al.*, 2006; *McWilliams et al.*, 2000] demonstrated that intermittent reconnection occurs at the magnetopause. *Badman et al.* [2013] actually detected the existence of bursty magnetic reconnection at Saturn's magnetopause even though the plasma β value is statistically unfavorable for the large scale magnetopause reconnection at Saturn [*Masters et al.*, 2012b]. The KH vortices at the non-linear stage can also induce localized reconnection [*Masters et al.*, 2010] as already demonstrated for Earth's magnetosphere [*Nykyri* *and Otto*, 2001; *Hasegawa et al.*, 2009]. We speculate that if the intermittent reconnection also takes place at Jupiter as well as Earth and Saturn, the auroral acceleration can accompany the X-ray emission.

7. Conclusion

Based on the multi-wavelength observations by Hisaki, XMM, and Chandra, we characterize our results for Jupiter's X-ray aurora as follows:

1. The X-ray count rate from Jupiter's auroral region varies by up to a factor of 3-4 over a time scale of 12 days and is positively correlated with the solar wind velocity.
2. The X-ray count rates in the XMM-Newton/EPIC-pn data are dominated by the oxygen band (0.5-0.7 keV) emission with a variable contribution from sulfur/carbon band (0.3-0.5 keV).
3. Over half of the X-ray events trace onto open field lines, and events that trace onto closed field lines are located mainly in the pre-noon to post-dusk sector.
4. The closed X-ray source field lines are magnetically connected with the magnetopause and outermost magnetospheric region.

From these observed characteristics, we conclude that:

5. The driving mechanism of the X-ray aurora is associated with the magnetopause and outermost magnetospheric region where the KH instability, magnetopause reconnection, and/or quasi-periodic energetic particle injection takes place.

Acknowledgments:

TK was supported by a grant-in-aid for Scientific Research from the Japan Society for the Promotion of Science (JSPS). The data of Hisaki satellite is archived in the Data Archives and Transmission System (DARTS) JAXA. Individuals may request the data by writing to Timoki Kimura (tomoki.kimura@riken.jp).

References

Arnaud, K. A. (1996), XSPEC: The first ten years, in Astronomical Data Analysis Software and Systems V, ASP Conf. Ser., vol. 101, edited by G. Jacoby and J. Barnes, p. 17, Astron. Soc. of the Pacific, San Francisco, Calif.

Badman, S. V., A. Masters, H. Hasegawa, M. Fujimoto, A. Radioti, D. Grodent,N. Sergis, M. K. Dougherty, and A. J. Coates (2013), Bursty magnetic reconnection at Saturn's magnetopause, *Geophys. Res. Lett.*, 40, 1027–1031, doi:10.1002/grl.50199.

F. Bagenal, A. Adriani, F. Allegrini, S.J. Bolton, B. Bonfond, E.J. Bunce, J.E.P. Connerney, S.W.H. Cowley, R.W. Ebert, G.R. Gladstone, C.J. Hansen, W.S. Kurth, S.M. Levin, B.H. Mauk, D.J. McComas, C.P. Paranicas, D. Santos-Costas, R.M. Thorne, P. Valek, J.H. Waite, P. Zarka (2014), Magnetospheric science objectives of the Juno mission, *Space Sci. Rev.*, 1-69, doi:10.1007/s11214-014-0036-8.

Bhardwaj, A., R. Elsner, R. Gladstone, T. E. Cravens, C. M. Lisse, K. Dennerl, G. Branduardi-Raymont, B. Wargelin, J. H Waite Jr., I. Robertson, N. Ostgaard, P. Beiersdorfer, S. L. Snowden, and V. Kharchenko (2007), X-rays from Solar System Objects, *Planetary and Space Science*, 55, pp. 1135-1189, doi:10.1016/j.pss.2006.11.009.

Bhardwaj, A., and G. R. Gladstone (2000), Auroral emissions of the giant planets, *Rev. Geophys.*, 38, 295– 353.

Baron, R. L., T. Owen, J. Connerney, T. Satoh, and J. Harrington (1996), Solar wind control of Jupiter's auroras, *Icarus*, *120*, 437 – 442, doi:10.1006/icar.1996.0063.

Bonfond, B., M. F. Vogt, J.-C. Gérard, D. Grodent, A. Radioti, and V. Coumans (2011), Quasi-periodic polar flares at Jupiter: A signature of pulsed dayside reconnections?, *Geophys. Res. Lett.*, *38*, L02104, doi:10.1029/2010GL045981.

Branduardi-Raymont, G., A. Bhardwaj, R. F. Elsner, G. R. Gladstone, G. Ramsay, P. Rodriguez, R. Soria, J. H.Waite Jr., and T. E. Cravens (2007), A study of Jupiter's aurorae with XMM-Newton, *Astron. Astrophys.*, 463, 761–774, doi:10.1051/0004-6361:20066406.

Branduardi-Raymont, G., R. F. Elsner, M. Galand, D. Grodent, T. E. Cravens, P. Ford, G. R. Gladstone, and J. H. Waite (2008), Spectral morphology of the X-ray emission from Jupiter's aurorae, *J. Geophys. Res.*, *113*, A02202, doi:10.1029/2007JA012600.

Branduardi-Raymont, G., et al. (2004), First observation of Jupiter by XMM-Newton, Astron. Astrophys., 424, 331, doi:10.1051/0004-6361:20041149.

Bunce, E. J., S. W. H. Cowley, and T. K. Yeoman (2004), Jovian cusp processes: Implications for the polar aurora, *J. Geophys. Res.*, 109, A09S13, doi:10.1029/2003JA010280.

Cassak, P. A., and A. Otto (2011), Scaling of the magnetic reconnection rate with symmetric shear flow, *Phys. Plasmas*, *18*, 074501, doi:10.1063/1.3609771.

Cecconi, B., and P. Zarka (2005), Model of a variable radio period for Saturn, *J. Geophys. Res.*, *110*, A12203, doi:10.1029/2005JA011085.

Clarke, J., *et al.* (2009), Response of Jupiter's and Saturn's auroral activity to the solar wind, *J. Geophys. Res. 114*, A05210, doi:10.1029/2008JA013694.

Cowley, S. W. H. and Bunce E. J., Origin of the main auroral oval in Jupiter's coupled magnetosphere-ionosphere system, *Planet., Space Sci.*, *49*, 1067, 2001.

Cravens, T. E., J. H. Waite, T. I. Gombosi, N. Lugaz, G. R. Gladstone, B. H. Mauk, and R. J. MacDowall (2003), Implications of Jovian X-ray emission for magnetosphere-ionosphere coupling, *J. Geophys. Res.*, 108(A12), 1465, doi:10.1029/2003JA010050.

Delamere, P. A., R. J. Wilson, S. Eriksson, and F. Bagenal (2013), Magnetic signatures of Kelvin-Helmholtz vortices on Saturn's magnetopause: Global survey, *J. Geophys. Res.*, 118, 393–404, doi:10.1029/2012JA018197.

Desroche, M., F. Bagenal, P. A. Delamere, and N. Erkaev (2012), Conditions at the expanded Jovian magnetopause and implications for the solar wind interaction, *J. Geophys. Res.*, 117, A07202, doi:10.1029/2012JA017621.

Dunn, W., G., Branduardi-Raymont , R., Elsner , M., Vogt , L., Lamy , P., Ford , A., Coates, G., Gladstone , C., Jackman , J., Nichols , I. Rae , A., Varsani , T., Kimura , K., Hansen , J., Jasinski (under review), The Impact of an ICME on the Jovian X-ray Aurora, *J. Geophys. Res.*, 2015JA021888.

Elsner, R. F., et al. (2005), Simultaneous Chandra X-ray, Hubble Space Telescope ultraviolet, and Ulysses radio observations of Jupiter's aurora, *J. Geophys. Res.*, 110, A01207, doi:10.1029/2004JA010717.

Galopeau, P., P. Zarka, and D. Le Que´au (1995), Source location of Saturn's kilometric radiation: The Kelvin-Helmholtz instability hypothesis, J. Geophys. Res., 100, 26,397–26,410.

Gladstone, G. R., et al. (2002), A pulsating auroral X-ray hot spot on Jupiter, *Nature*, 415(6875), 1000–1003.

Gurnett, D. A., et al. (2002), Control of Jupiter's radio emission and aurorae by the solar wind, *Nature*, *415*, 985-987, doi:10.1038/415985a.

Hasegawa, H., A. Retino, A. Vaivads, Y. Khotyaintsev, M. Andre, T. K. M. Nakamura, W.-L. Teh, B. U. O. Sonnerup, S. J. Schwartz, Y. Seki, M. Fujimoto, Y. Saito, H. Reme, and P. Canu, Kelvin-Helmholtz waves at the Earth's magnetopause: Multiscale development and associated reconnection, J. Geophys. Res., 114, A12207, doi:10.1029/2009JA014042, 2009.

Hess, S. L. G., B. Bonfond, P. Zarka, and D. Grodent (2011), Model of the Jovian magnetic field topology constrained by the Io auroral emissions, J. Geophys. Res., 116, A05217, doi:10.1029/2010JA016262.

Hill, T. W., The jovian auroral oval, *J. Geophys. Res.*, *106*, 8101, 2001.

Hui, Y., D. R. Schultz, V. A. Kharchenko, A. Bhardwaj, G. Branduardi-Raymont, P. C. Stancil, T. E. Cravens, C. M. Lisse, and A. Dalgarno (2010), Comparative analysis and variability of the Jovian X-ray spectra detected by the Chandra and XMM-Newton observatories, J. Geophys. Res., 115, A07102, doi:10.1029/2009JA014854.

Hui, Y., D. R. Schultz, V. Kharchenko, P. Stancil, T. E. Cravens, C. M. Lisse, and A. Dalgarno, The ion induced charge exchange x-ray emission of the Jovian auroras: Magnetospheric or solar wind origin?, *Astrophys. J.*, 702, L158, doi:10.1088/0004637X/702/2/L158, 2009.

Joy, S. P., M. G. Kivelson, R. J. Walker, K. K. Khurana, C. T. Russell, and T. Ogino, Probabilistic models of the Jovian magnetopause and bow shock locations, J. Geophys. Res., 107(A10), 1309, doi:10.1029/2001JA009146, 2002.

Kharchenko, V., Weihong Liu, and A. Dalgarno (1998), X-ray and EUV emission spectra for oxygen ions precipitating into the Jovian atmosphere, *J. Geophys. Res.*, 102(A11), 26687.

Kharchenko, V., A. Dalgarno, D. R. Schultz, and P.C. Stancil (2006), Ion emission spectra in the Jovian X-ray aurora, *Geophys. Res. Lett.*, 33, L11105, doi:10.1029/2006GL026039.

Kharchenko, V., A. Bhardwaj, A. Dalgarno, D. R. Schultz, and P. C. Stancil (2008), Modeling spectra of the north and south Jovian X-ray auroras, *J. Geophys. Res.*, 113, A08229, doi:10.1029/2008JA013062.

Kimura, T. et al. (2015), Transient internally-driven aurora at Jupiter discovered by Hisaki and Hubble Space Telescope, Geophys. Res. Lett., *42*, doi:10.1002/2015GL063272.

Kimura, T., B. Cecconi, P. Zarka, Y. Kasaba, F. Tsuchiya, H. Misawa, and A. Morioka (2012), Polarization and direction of arrival of Jovian quasiperiodic bursts observed by Cassini, J. Geophys. Res., 117, A11209, doi:10.1029/2012JA017506.

Kimura, T., F. Tsuchiya, H. Misawa, A. Morioka, and H. Nozawa (2008), Radiation characteristics of quasi-periodic radio bursts in the Jovian high latitude region, Planetary and Space Science, 56, 1967–1976.

Kimura, T., F. Tsuchiya, H. Misawa, A. Morioka, and H. Nozawa (2010), Occurrence statistics and ray tracing study of Jovian quasiperiodic radio bursts observed from low latitudes, J. Geophys. Res., 115, A05217, doi:10.1029/2009JA014647.

MacDowall, R. J., M. L. Kaiser, M. D. Desch, W. M. Farrell, R. A. Hess, and R. G. Stone (1993), Quasiperiodic Jovian radio bursts: Observations from the Ulysses radio and plasma wave experiment, *Planet. Space Sci.*, 41, 1059–1072, doi:10.1016/0032-0633(93)90109-F.

Masters, A., et al. (2010), Cassini observations of a Kelvin-Helmholtz vortex in Saturn’s outer magnetosphere, J. Geophys. Res., 115, A07225, doi:10.1029/2010JA015351.

Masters, A., N. Achilleos, J. C. Cutler, A. J. Coates, M. K. Dougherty, and G. H. Jones (2012a), Surface waves on Saturn's magnetopause, Planet. Space Sci., 65, 109121, doi:10.1016/j.pss.2012.02.007.

Masters, A., J. P. Eastwood, M. Swisdak, M. F. Thomsen, C. T. Russell, N. Sergis, F. J. Crary, M. K. Dougherty, A. J. Coates, and S. M. Krimigis (2012b), The importance of plasma β conditions for magnetic reconnection at Saturn's magnetopause, Geophys. Res. Lett., 39, L08103, doi:10.1029/2012GL051372.

McKibben, R., J. Simpson, and M. Zhang (1993), Impulsive bursts of relativistic electrons discovered during Ulysses' traversal of Jupiter's dusk-side magnetosphere, *Planet. Space Sci.*, 41(11–12), 1041–1058, doi:10.1016/0032-0633(93)90108-E.

McWilliams, K. A., T. K. Yeoman, and G. Provan (2000), A statistical survey of dayside pulsed ionospheric flows as seen by the CUTLASS Finland HF radar, Ann. Geophys., 18, 445-453, doi:10.1007/s00585-000-0445-8.

Metzger, A. E., D. A. Gilman, J. L. Luthey, K. C. Hurley, H. W. Schnopper, F. D. Seward, and J. D. Sullivan (1983), The detection of X rays from Jupiter, J. Geophys. Res., 88(A10), 7731–7741, doi:10.1029/JA088iA10p07731.

Morioka, A., H. Nozawa, H. Misawa, F. Tsuchiya, Y. Miyoshi, T. Kimura, and W. Kurth (2006), Rotationally driven quasiperiodic radio emissions in the Jovian magnetosphere, *J. Geophys. Res.*, *111*, A04223, doi:10.1029/2005JA011563.

Murray et al. (2000), In-flight Performance of the Chandra High Resolution Camera, *Proc. SPIE* 4012, X-Ray Optics, Instruments, and Missions III, 68, doi:10.1117/12.391591.

Nichols, J. D., E. J. Bunce, J. T. Clarke, S. W. H. Cowley, J.-C. Gérard, D. Grodent, and W. R. Pryor (2007), Response of Jupiter's UV auroras to interplanetary conditions as observed by the Hubble Space Telescope during the Cassini flyby campaign, *J. Geophys. Res.*, *112*, A02203, doi:10.1029/2006JA012005.

Nichols, J. D., J. T. Clarke, J.-C. Gérard, D. Grodent, and K. C. Hansen (2009), Variation of different components of Jupiter's auroral emission, *J. Geophys. Res.*, *114*, A06210, doi:10.1029/2009JA014051.

Nykyri, K., and A. Otto, Plasma transport at the magnetospheric boundary due to reconnection in Kelvin-Helmholtz vortices, Geophys. Res. Lett., 28, 3565-3568, 2001.

Ozak, N., D. R. Schultz, T. E. Cravens, V. Kharchenko, and Y. W. Hui, Auroral x-ray emission at Jupiter: Depth effects, *J. Geophys. Res.*, 115, A11306, doi:10.1029/2010JA015635, 2010.

Ozak, N., T. E. Cravens, and D. R. Schultz, Auroral ion precipitation at Jupiter: Predictions for Juno, *Geophys. Res. Lett.*, 40, doi:10.1002/grl.50812, 2013.

Prangé, R., G. Chagnon, M. G. Kivelson, T. A. Livengood, and W. Kurth (2001), Temporal monitoring of Jupiter's auroral activity with IUE during the Galileo mission. Implications for magnetospheric processes, *Planet. Space Sci.*, *49*, 405–415, doi:10.1016/S0032-0633(00)00161-6.

Prangé, R., L. Pallier, K. C. Hansen, R. Howard, A. Vourlidas, R. Courtin and C. Parkinson (2004), An interplanetary shock traced by planetary auroral storms from the Sun to Saturn, *Nature*, *432*, 78-81, doi:10.1038/nature02986.

Pryor, W. R., et al. (2005), Cassini UVIS observations of Jupiter's auroral variability, *Icarus* *178*, 312-326, doi:10.1016/j.icarus.2005.05.021.

Raeder, J., Flux Transfer Events: 1. generation mechanism for strong southward IMF, *Ann. Geophys.*, 24, 381-392, 2006.

Roussos, E., N. Krupp, D.G. Mitchell, C. Paranicas, S.M. Krimigis, M. Andriopoulou, B. Palmaerts, W.S. Kurth, S.V. Badman, A. Masters, M.K Dougherty (2015), Quasi-periodic injections of relativistic electrons in Saturn's outer magnetosphere, Icarus, in press, doi:10.1016/j.icarus.2015.04.017.

Strüder et al. (2001), The European Photon Imaging Camera on XMM-Newton: The pn-CCD camera, *A&A*, 365, L18-L26, doi:10.1051/0004-6361:20000066.

Swisdak, M., M. Opher, J. F. Drake, and F. Alouani Bibi (2010), The vector direction of the interstellar magnetic field outside the heliosphere, *Astrophys. J.*, 710, 1769–1775, doi:10.1088/0004-637X/710/2/1769.

Tao, C., R. Kataoka, H. Fukunishi, Y. Takahashi, and T. Yokoyama (2005), Magnetic field variations in the Jovian magnetotail induced by solar wind dynamic pressure enhancements, *J. Geophys. Res.*, *110*, A11208, doi:10.1029/2004JA010959.

Tsuchiya, F., M. Kagitani, N. Terada, Y. Kasaba, I. Yoshikawa, G. Murakami, K. Sakai, T. Homma, K. Yoshioka, A. Yamazaki, K. Uemizu, T. Kimura, and M. Ueno (2010), Plan for observing magnetospheres of outer planets by using the EUV spectrograph onboard the SPRINT-A/EXCEED mission, *Adv. Geosci*,. *25*, 57-71, doi:10.1142/9789814355377_0005.

Turner et al. (2001), The European Photon Imaging Camera on XMM-Newton: The MOS Cameras, *A&A*, *365*, L27-L35, doi:10.1051/0004-6361:20000087.

Vogt, M. F., E. J. Bunce, M. G. Kivelson, K. K. Khurana, R. J. Walker, A. Radioti, B. Bonfond, and D. Grodent (2015), Magnetosphere-ionosphere mapping at Jupiter: Quantifying the effects of using different internal field models, *J. Geophys. Res. Space Physics*, *120*, doi:10.1002/2014JA020729.

Vogt, M. F., M. G. Kivelson, K. K. Khurana, R. J. Walker, B. Bonfond, D. Grodent, and A. Radioti (2011), Improved mapping of Jupiter's auroral features to magnetospheric sources, *J. Geophys. Res.*, *116*, A03220, doi:10.1029/2010JA016148.

Yoshioka, K., G. Murakami, A. Yamazaki, F. Tsuchiya, M. Kagitani, T. Sakanoi, T. Kimura, K. Uemizu, K. Uji, I. Yoshikawa (2013), The extreme ultraviolet spectroscope for planetary science, EXCEED, *Planet. Space Sci.*, *85*, 250-260, doi:10.1016/j.pss.2013.06.021.

Figures:

Figure 1. (a) Jupiter's X-ray image in Jupiter-centric coordinates measured by CXO/HRC and (b) that measured by XMM-Newton/EPIC-pn during Jupiter's observing campaign in Apr 2014. The spatial scale is the same in panel (a) and (b). The green rectangle in panel (b) is located at the northern auroral region aligned with Jupiter's equator. The auroral X-ray photons from the green-framed region are extracted for spectral analysis. The green circle in panel (b) indicates the background region from which photon count rate and spectra of the solar radiation are extracted for the background noise reduction.

Figure 2. Polar plot of the source location of the X-ray photons in the System III coordinates where the background colored contours indicate the magnitude of the magnetic field strength. The X-ray events were extracted from the full HRC dataset on Apr 8-20 during the Jupiter observing campaign. The field strength is provided by the VIPAL model [*Hess et al.*, 2011]. The x axis is in the meridian plane at System III longitude of 90°, and the y axis is in the meridian plane of 0°. Interval of the latitudinal grids is 10°. The orange, blue, and white lines indicate latitudes from which magnetic field lines map to radial distances of 15, 30, and 120 Rj in the equatorial magnetosphere, respectively. Mapping of these radial distances to the polar ionosphere was done using the *flux equivalence mapping model* by *Vogt et al.* [2011, 2015]. Sub-solar longitude in the model is set to 180°. Red points indicate the 'core' region where the photon density is the highest. Blue points indicate from the 'halo' region, where the photons are more sparse, surrounding the core region.

Figure 3. Background-subtracted spectra observed by XMM-Newton/EPIC-pn on (a) Apr 15 and (b) Apr 20, 2014. Horizontal axis shows photon energy. Vertical axis is the differential count rate. Crosses show measured count rate with error bars which are estimated based on Poisson statistics. The solid line shows the best-fit model.

Figure 4. Time variations in the EUV, X-ray aurora and the modeled solar wind. (a) EUV total auroral power (900-1480 Å) extracted from Hisaki/EXCEED imaging spectral data, taken when Hisaki's CML is 100°-250°. Integration times are 10 minutes. Vertical error bars are evaluated based on the Poisson statistics. (b) CXO/HRC X-ray auroral count rates extracted from the core (red circles) and halo (blue triangles) regions. (c) XMM-Newton/EPIC-pn 0.5-0.7 keV count rates and (d) XMM-Newton/EPIC-pn 0.3-0.5 count rates. Integration times for panels (b), (c) and (d) are ~40 ks, i.e., the full length of the observations. All error bars are based on the Poisson statistics. (e) Solar wind radial velocity, and (f) dynamic pressure extrapolated from those measured at Earth's orbit. The extrapolation is performed based on the magnetohydrodynamic (MHD) simulation developed by *Tao et al.* [2005].

Figure 5. Scatter plots of the X-ray count rates and solar wind parameters. (a) The core count rates as a function of the solar wind velocity. The solar wind velocity is averaged over ±48 hours from the count rate measurement time. The error bars in the velocity are standard deviations of the time series that span ±48 hours from the count rate measurement time. The error bars in the count rate are estimated based on the photon statistics. The core count rate is temporally lagged by 27 hours when the magnitude of CCC is the largest for time lags from -48 to +48 hours. The largest magnitude CCC is displayed above the scatter plot with the time lag.

Figure 6. The distribution of mappings of CXO/HRC X-ray events on the equatorial plane in JSE coordinates. Red and blue crosses indicate the closed field lines corresponding to the core and halo regions, respectively. The X-ray source field lines are mapped based on the *flux equivalence mapping model* by *Vogt et al.* [2011, 2015]. The solid red line indicates the nominal location of magnetopause as modeled by a quadratic curve defined in *Joy et al.* [2002]. The magnetosphere is assumed to be an uncompressed with a solar wind dynamic pressure of 0.04 nPa.

Figure 7. (a) Local time (LT) distribution of the X-ray mappings for closed field lines at 15-90 Rj on the equatorial plane. The filled blue histogram shows the LT distributions for the closed field lines in the halo. The filled red histogram is the LT distribution in the core, stacked on the halo's histogram. (b) LT distribution of the occurrence probability for the halo and core. The black broken line is the cumulative observation time for each local time sector normalized by the peak value at LT 12. Filled blue and red histograms are the occurrence probabilities of the halo and core, respectively, with the core histogram stacked on the halo histogram. These histograms are calculated by dividing the histogram from (a) by the cumulative time. Each value is normalized by the sum of halo and core probabilities at LT 12-13.

Figure 8. (a) The number of the auroral X-ray events as a function of observer's CML. The filled blue histogram shows the CML distribution for the halo. The filled red histogram is the CML distribution of the core, stacked on the halo's histogram. (b) The occurrence probability of the halo and core as functions of CML. The black broken line is the cumulative observation time of the polar cap region. The filled blue and red histograms are the occurrence probabilities of the halo and core, respectively. The core histogram is stacked on the halo histogram. These histograms are calculated by dividing the histogram from (a) by the cumulative time. Each value is normalized by the sum of the halo and core probabilities at CML 120°-150°.

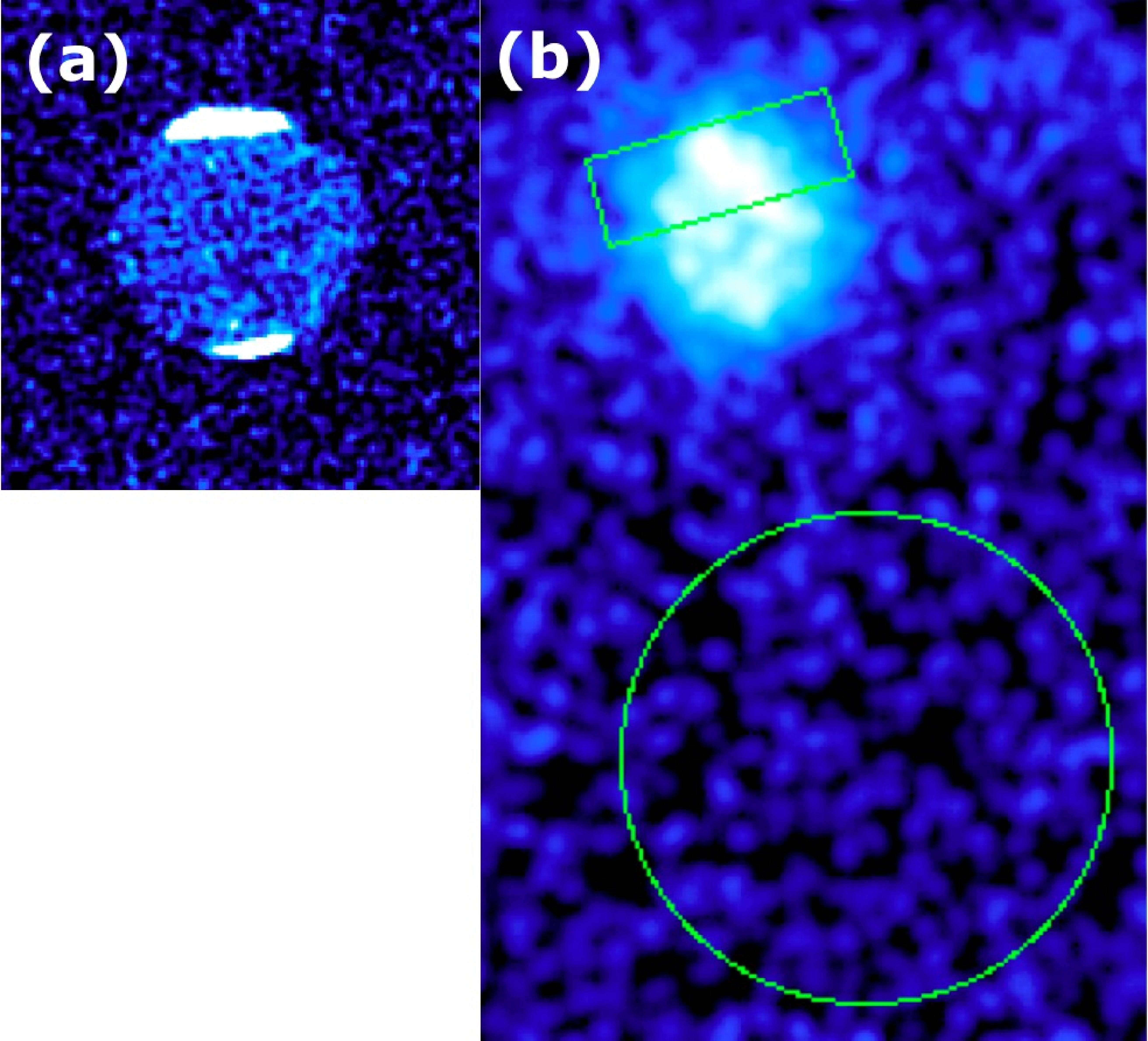
(a)
(b)

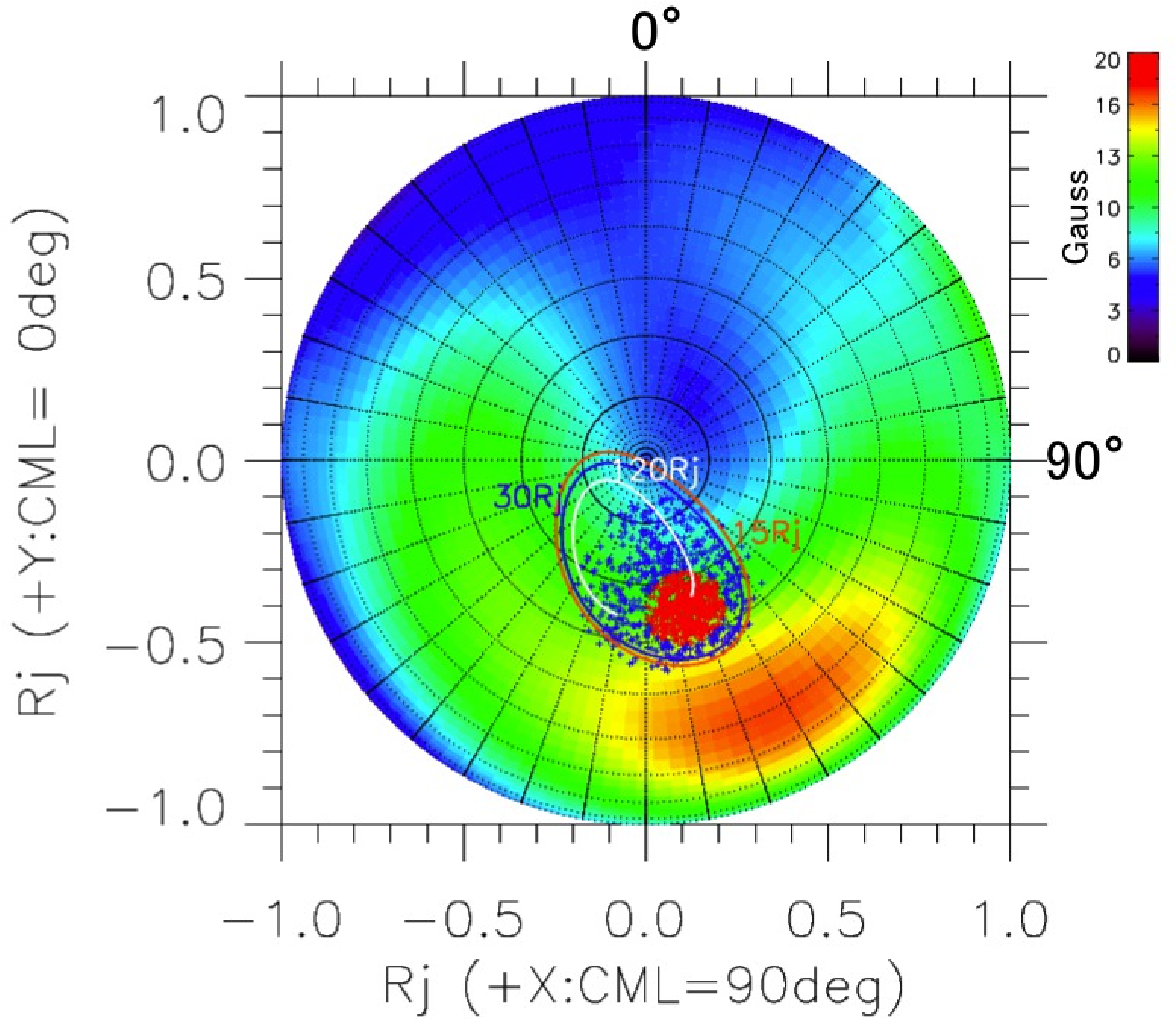

0°
90°
1.0
0.5
0.0
−0.5
−1.0
−1.0
−0.5
0.0
0.5
1.0
Rj (+Y:CML= 0deg)
Rj (+X:CML=90deg)
20Rj
30Rj
15Rj
Gauss
20
16
13
10
6
3
0

data and folded model

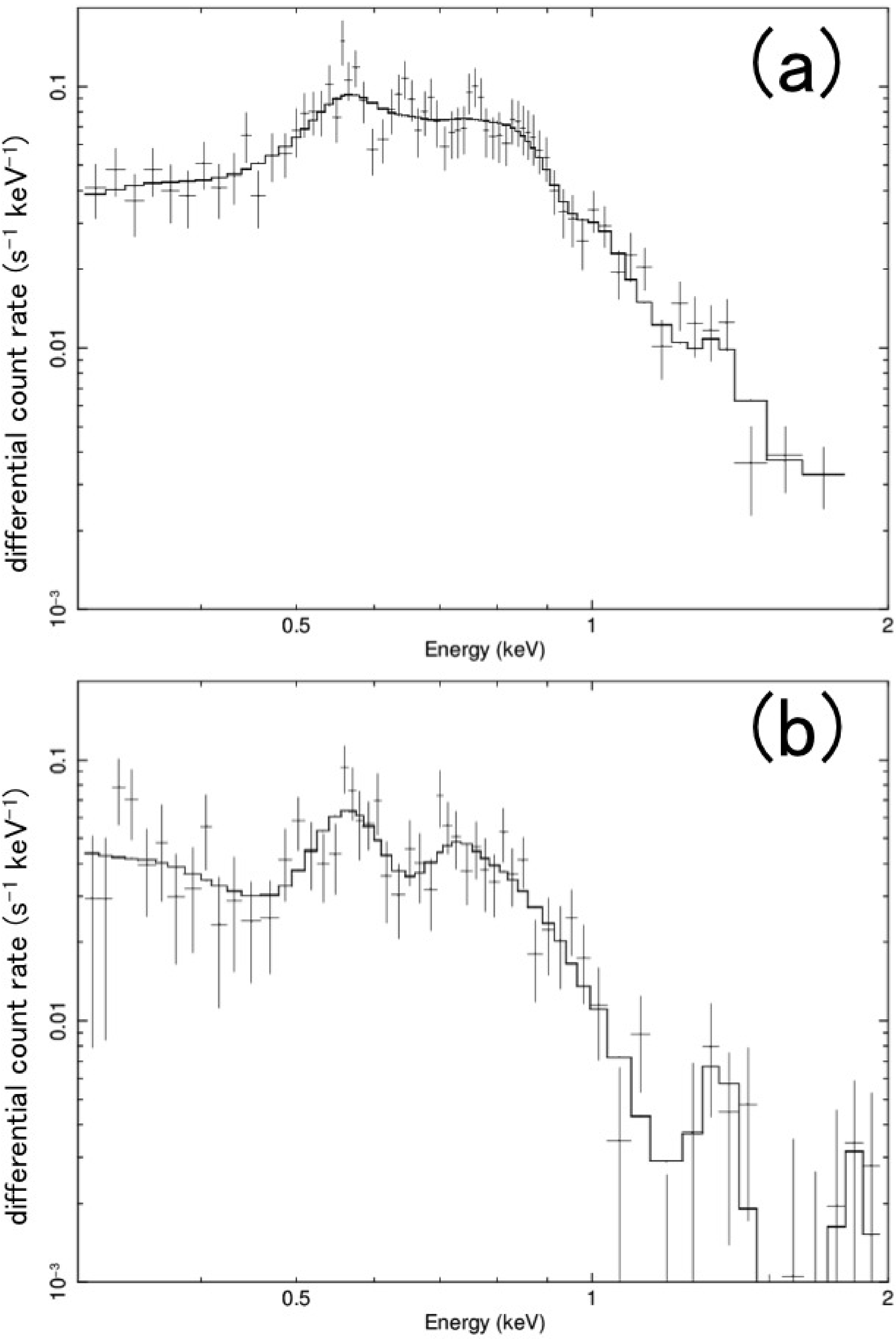

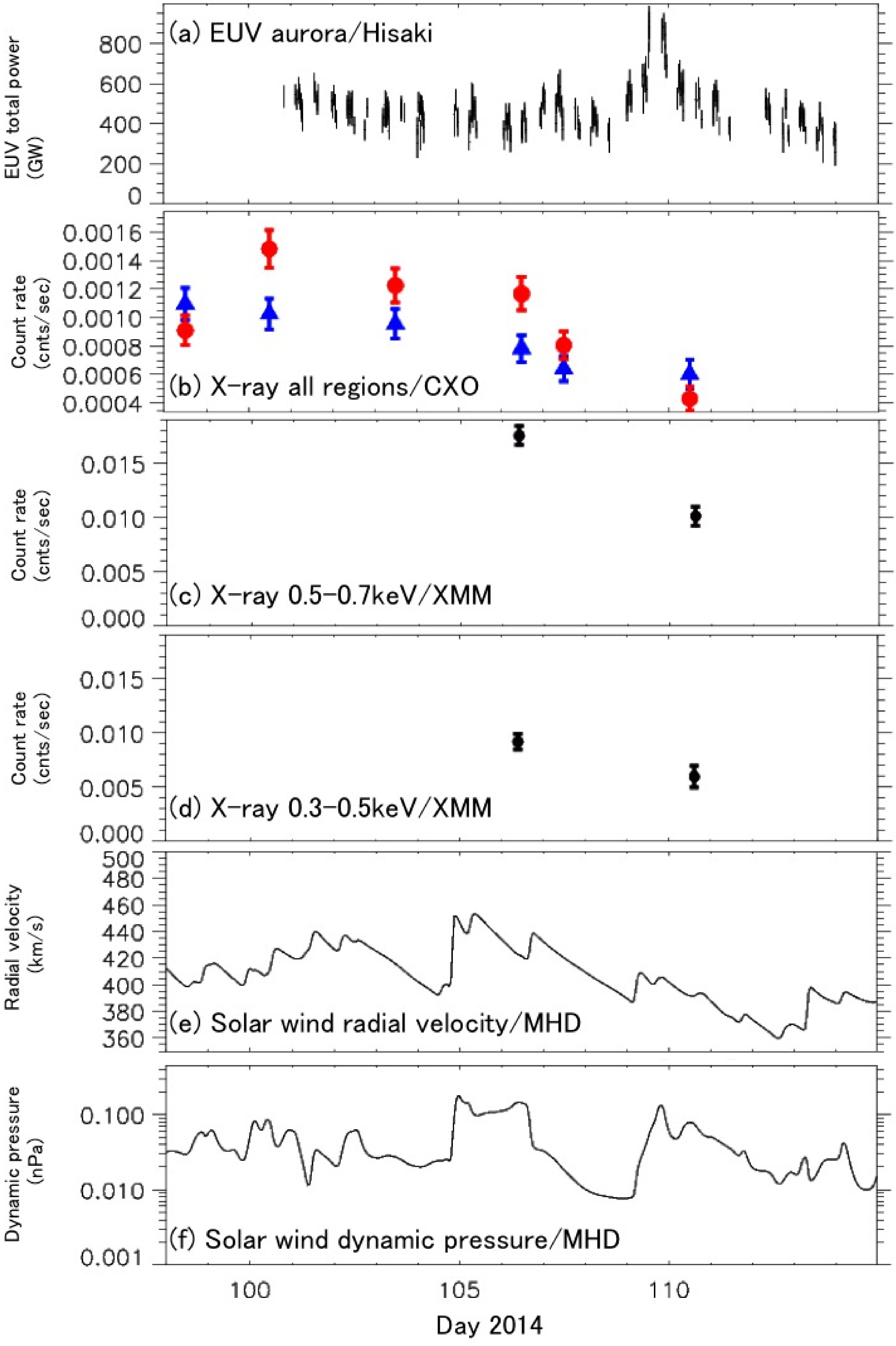

(a) EUV aurora/Hisaki
EUV total power (GW)
800
600
400
200
0
(b) X-ray all regions/CXO
Count rate (cnts/sec)
0.0016
0.0014
0.0012
0.0010
0.0008
0.0006
0.0004
(c) X-ray 0.5-0.7keV/XMM
Count rate (cnts/sec)
0.015
0.010
0.005
0.000
(d) X-ray 0.3-0.5keV/XMM
Count rate (cnts/sec)
0.015
0.010
0.005
0.000
(e) Solar wind radial velocity/MHD
Radial velocity (km/s)
500
480
460
440
420
400
380
360
(f) Solar wind dynamic pressure/MHD
Dynamic pressure (nPa)
0.100
0.010
0.001
100
105
110
Day 2014

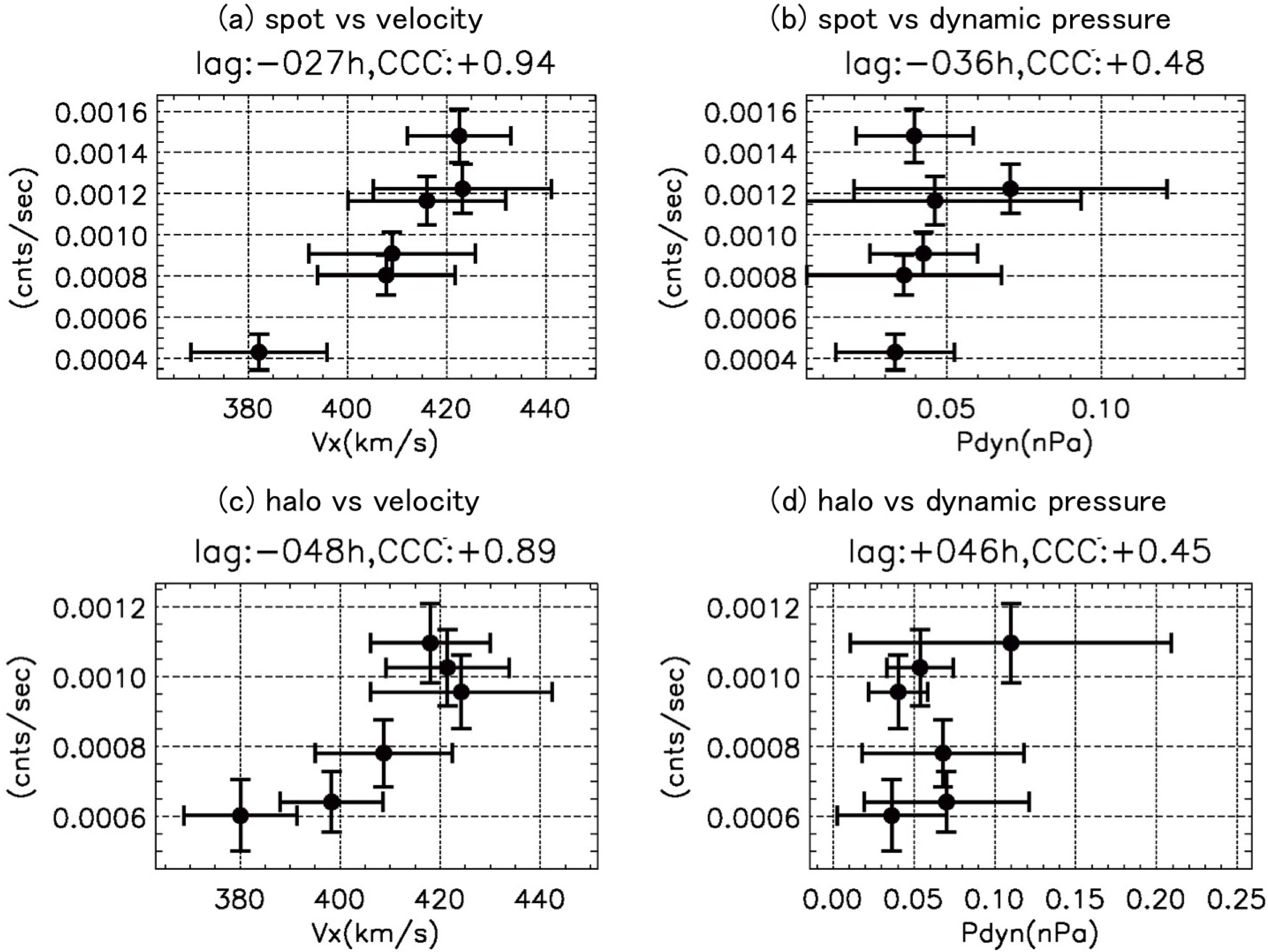
(a) spot vs velocity
lag:−027h,CCC:+0.94
0.0016
0.0014
0.0012
0.0010
0.0008
0.0006
0.0004
(cnts/sec)
380
400
420
440
Vx(km/s)
(b) spot vs dynamic pressure
lag:−036h,CCC:+0.48
0.0016
0.0014
0.0012
0.0010
0.0008
0.0006
0.0004
(cnts/sec)
0.05
0.10
Pdyn(nPa)
(c) halo vs velocity
lag:−048h,CCC:+0.89
0.0012
0.0010
0.0008
0.0006
(cnts/sec)
380
400
420
440
Vx(km/s)
(d) halo vs dynamic pressure
lag:+046h,CCC:+0.45
0.0012
0.0010
0.0008
0.0006
(cnts/sec)
0.00
0.05
0.10
0.15
0.20
0.25
Pdyn(nPa)

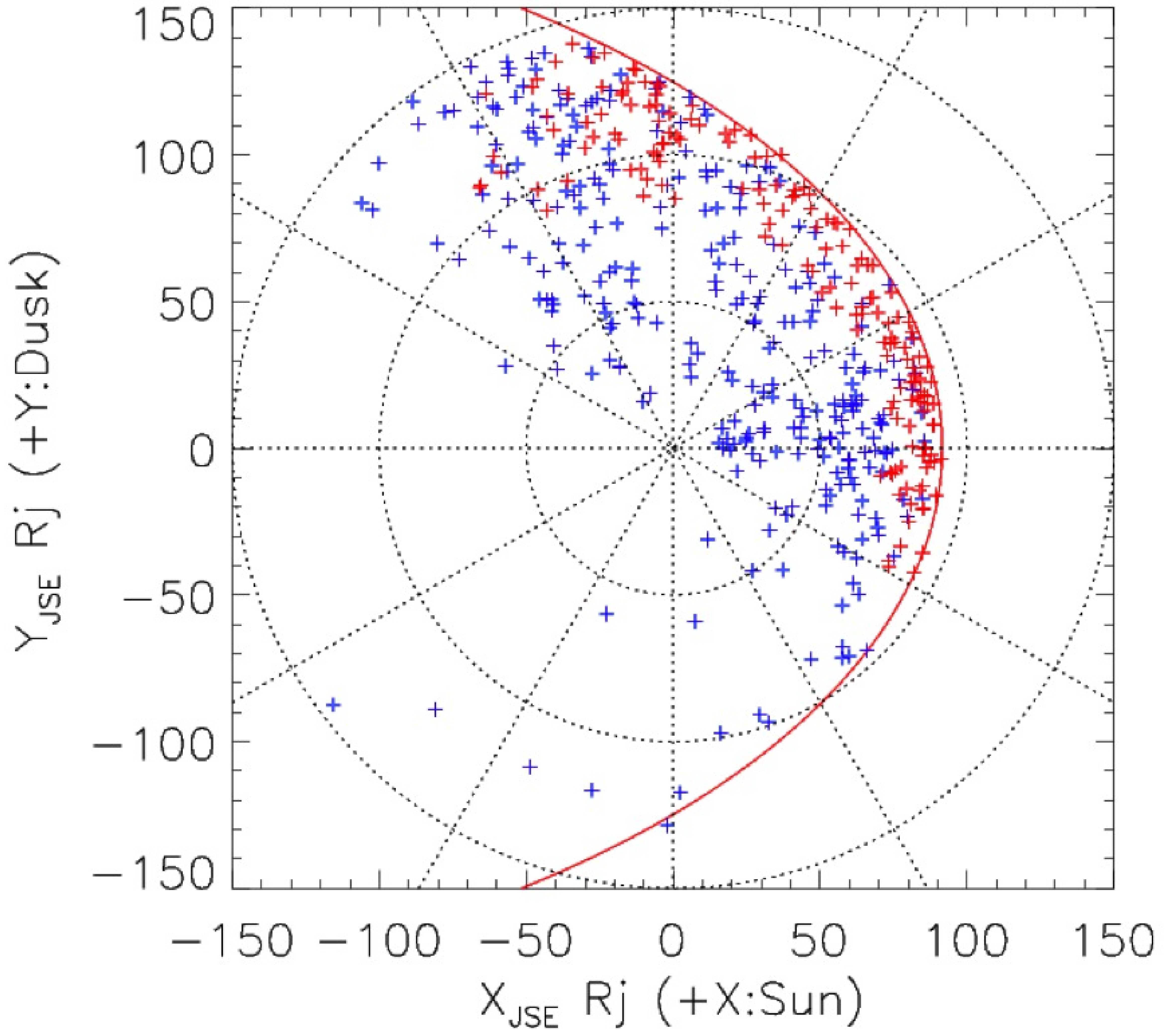
150
100
50
0
−50
−100
−150
Y_{JSE} Rj (+Y:Dusk)
−150 −100 −50 0 50 100 150
X_{JSE} Rj (+X:Sun)

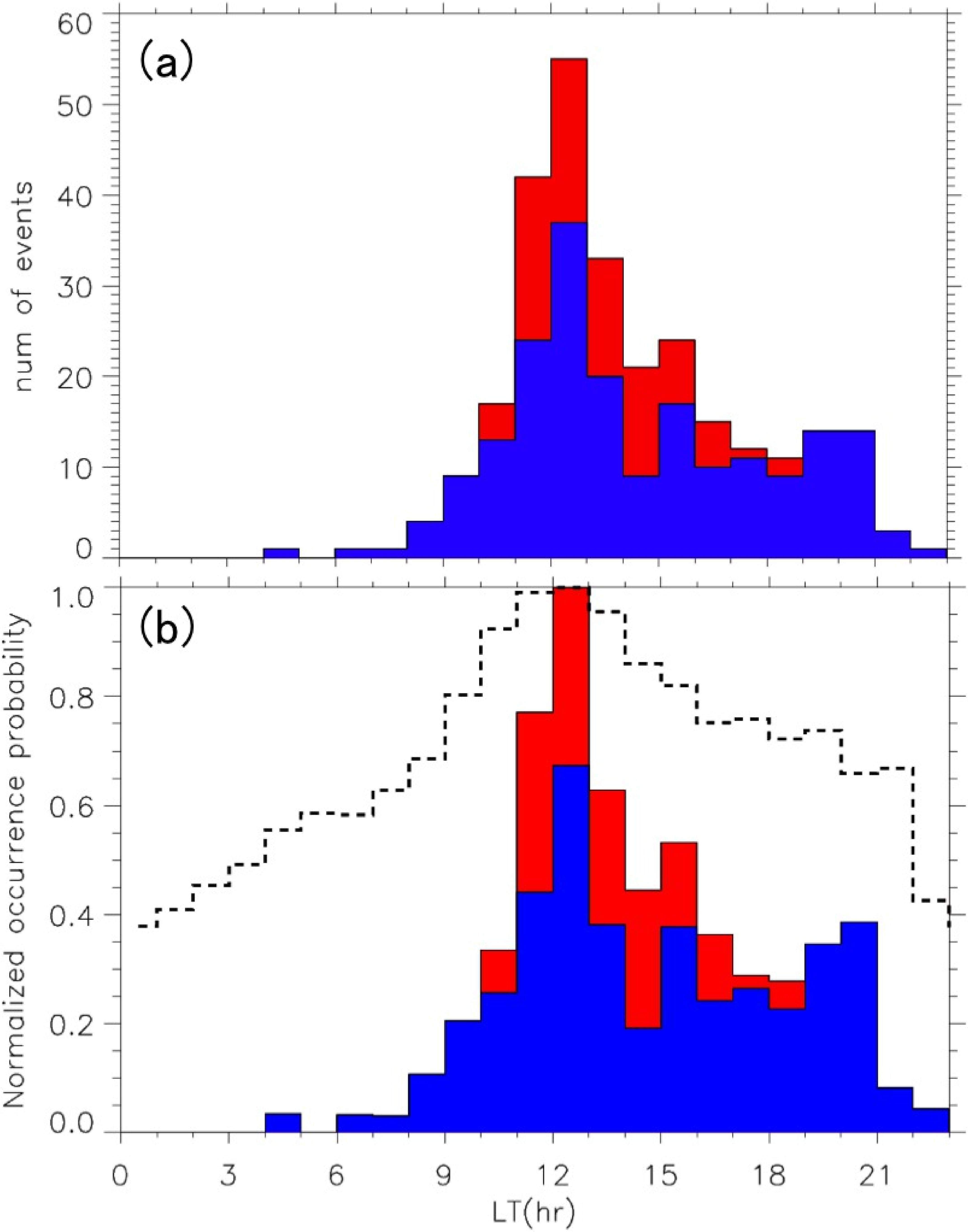

(a)
num of events
0
10
20
30
40
50
60
(b)
Normalized occurrence probability
0.0
0.2
0.4
0.6
0.8
1.0
0
3
6
9
12
15
18
21
LT(hr)

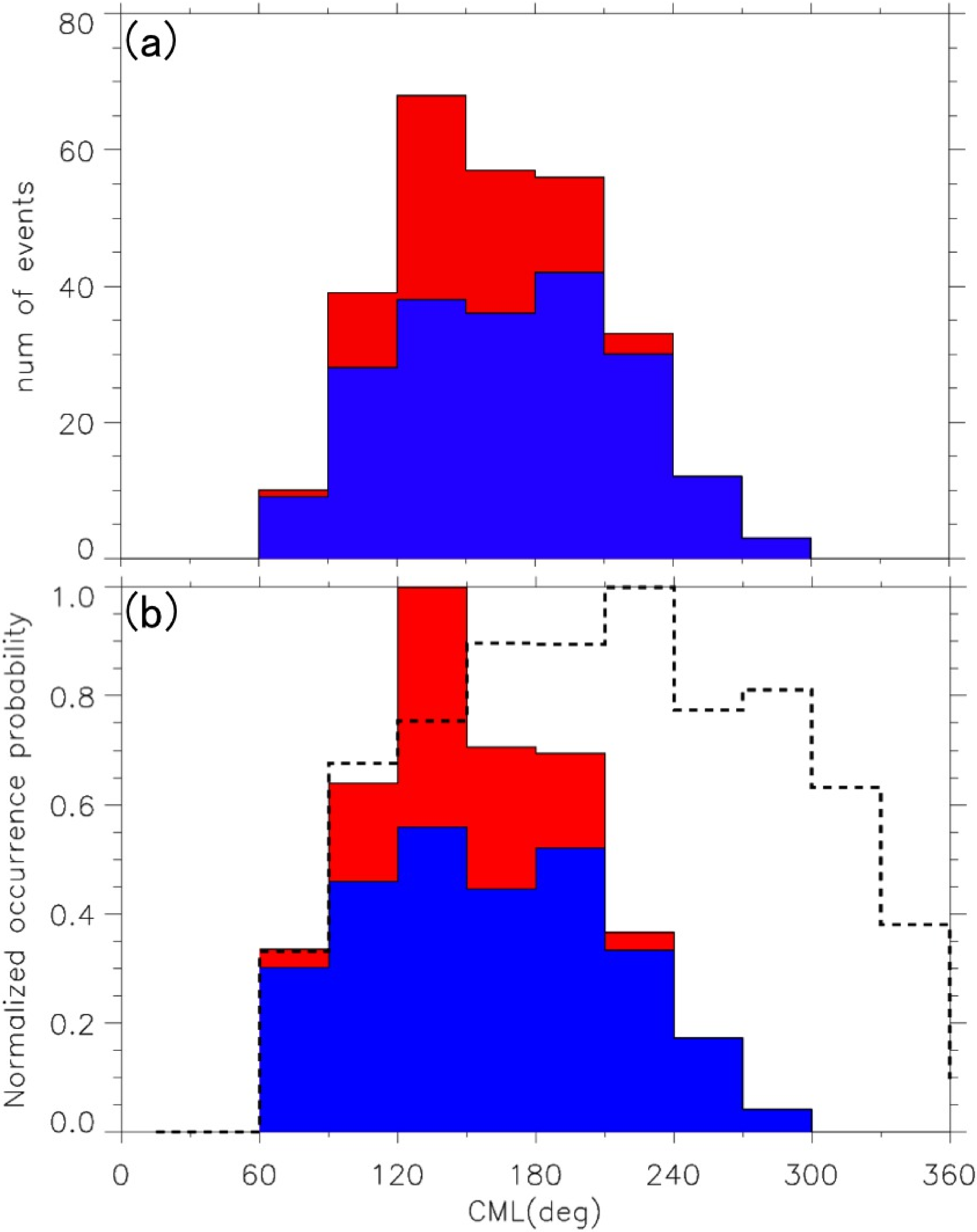

(a)
num of events
80
60
40
20
0
(b)
Normalized occurrence probability
1.0
0.8
0.6
0.4
0.2
0.0
0
60
120
180
240
300
360
CML(deg)